Investigating Rayleigh wave anisotropy in faulted media with three-component beamforming: insights from numerical models and applications for geothermal exploration

Heather Kennedy[a] (h.kennedy.21@abdn.ac.uk), Claudia Finger[b] (claudia.finger@ieg.fraunhofer.de), Katrin Löer[c] (K.Loer@tudelft.nl), Amy Gilligan[a] (amy.gilligan@abdn.ac.uk)

[a]University of Aberdeen, School of Geosciences, Aberdeen, AB24 3UE, Aberdeenshire, United Kingdom

[b]Fraunhofer IEG, Fraunhofer Institution for Energy Infrastructures and Geothermal Systems IEG, Bochum, Germany

[c]Delft University of Technology, School of Civil Engineering and Geosciences, Delft, Netherlands

This is a non-peer reviewed preprint submitted to EarthArXiv.

This pre-print has been submitted to Wave Motion for peer-review.

Highlights

Investigating Rayleigh wave anisotropy in faulted media with three-component beamforming: insights from numerical models and applications for geothermal exploration

Heather Kennedy, Claudia Finger, Katrin Löer, Amy Gilligan

- Structural anisotropy and azimuthal anisotropy of synthetic Rayleigh waves do not always align.
- Smaller velocity contrasts result in more complex/ambiguous anisotropy.
- Slow directions give a better indication of the fault strike when the velocity contrast is small.
- Effect of array design on anisotropy analysis is small when the velocity contrast is large.

Investigating Rayleigh wave anisotropy in faulted media with three-component beamforming: insights from numerical models and applications for geothermal exploration

Heather Kennedy[a], Claudia Finger[b], Katrin Löer[c], Amy Gilligan[a]

[a] *University of Aberdeen, School of Geosciences, Aberdeen, AB24 3UE, Aberdeenshire, United Kingdom*
[b] *Fraunhofer IEG, Fraunhofer Institution for Energy Infrastructures and Geothermal Systems IEG, Bochum, Germany*
[c] *Delft University of Technology, Delft University of Technology, Delft, Netherlands*

Abstract

Rayleigh waves are prevalent in the ambient seismic noise wavefield and are thus often exploited in passive seismic methods to characterise the near subsurface. In fractured or faulted media, Rayleigh waves show azimuthal anisotropy that could provide information on the fault properties. However, the exact relationship between Rayleigh wave anisotropy and true anisotropic structures is not well known. This study used a three-component (3C) beamforming toolbox to analyse numerical full waveform seismic wave propagation from conceptual models of fractured media. We identify Rayleigh waves in the synthetic data, compare observed Rayleigh wave anisotropy to structural anisotropy, and assess the effect array design and source locations have on Rayleigh wave analysis and observed anisotropy. Numerical analysis shows that the smaller the velocity contrast between fault and surrounding rock, the more complex the anisotropic response. We find that the slow directions of Rayleigh wave propagation can be a better indicator of fault strike than the fastest direction, when the velocity contrast between the two media are small.

Keywords: Numerical modelling, fractured media, Three-component beamforming, geothermal application, Rayleigh wave anisotropy

1. Introduction

Ambient seismic noise is a widely available and cheap seismic source that provides significant surface wave energy and is also present where natural seismicity is low [1]. Rayleigh waves are a type of surface wave that can propagate through the subsurface and provide observed anisotropy of the subsurface. Array-based techniques, such as beamforming, can be used to analyse ambient seismic noise data and assess Rayleigh wave anisotropy in fractured media.

One application for three-component (3C) beamforming of ambient seismic noise analysis of numerical data is geothermal fields. Geothermal fields are essential for the energy transition [2]. In geothermal exploration, the circulation of hydrothermal fluid is essential [3]. Fractures and faults provide an invaluable source of secondary permeability for this circulation of hydrothermal flow [4]. Observed anisotropy, which is usually a mix of intrinsic and extrinsic anisotropy [5], is a feature of the medium, and when seismic waves travel through an anisotropic medium they also show anisotropic features, such as velocity variations with direction or polarization (as in shear wave splitting), depending on spatial scale and seismic wavelength [5]. Observed anisotropy can indicate the presence of faults in the subsurface, providing insight into the degree of secondary permeability within a geothermal field.

Previous studies [6; 7; 8; 9] have shown a relation between anisotropy at depth and fractures. Kennedy et al. [6] used three-component (3C) beamforming of ambient seismic noise to look at Rayleigh wave anisotropy, as a function of frequency, and related the fast directions of Rayleigh waves to fault variations at depth. This was based on the hypothesis that Rayleigh waves would travel faster parallel to the fault rather than perpendicular to the fault due to changes in the elastic constants of the structures in the surrounding lithology compared to the fault itself [10; 11; 12]. The fastest observed velocities correpsond to specific azimuths, thus providing an indication of the strike of a fault at different depths.

Luo and Yao [7] derive a three-dimensional (3D) high-resolution upper crustal azimuthally anisotropic model of shear wave velocity using surface wave (specifically Rayleigh wave) dispersion data from ambient seismic noise. They found that fast directions of azimuthal anisotropy were consistent with local geological units, seeing variations at different depths. Li and Peng [8] use shear wave splitting (SWS), a method that analyses the splitting of horizontally and vertically polarised shear waves (shear horizontal (SH) and

shear vertical (SV), respectively) in anisotropic media [13], to look at fast directions related to regional compressional stress and local fault strikes. They found that some near-fault stations display fast directions parallel to the fault strikes [8]. Boness and Zoback [9] measured SWS using microearthquakes to distinguish between stress induced anisotropy or structural anisotropy, they found that fast directions were parallel to the strike of structural anisotropy (such as faults) and that the fast directions were perpendicular to stress-induced anisotropy (such as microcracks) [9].

In this study, we test the relation of fault strike and fast directions in Rayleigh wave anisotropy using three-component (3C) beamforming of synthetic data. Numerical modelling of seismic wave propagation is done to assess Rayleigh wave behaviour, anisotropy changes in different geological settings, array design and the impact of source locations; velocity contrasts and density. 3C beamforming (first formulated by [14; 15; 16; 17]) of ambient seismic noise is an array-based technique which enables the determination of propagation directions and propagation velocities, and, thus, allows for the inference of surface wace anisotropy. The 3C beamforming method used in this study extracts the polarisation, phase velocities, and azimuths of different wave types in the seismic wavefield as a function of frequency [18]. Furthermore, it can be used for transient wave analysis from a single point source as well, as typically done in earthquake seismology [19]. Here, we focus on azimuthal anisotropy observed as variations in surface wave velocity as a function of propagation direction. An anisotropy curve is fitted to the azimuth-velocity estimates obtained from beamforming (as in [1; 20]) and by assessing the slow and fast directions of these curves, we should be able to infer the strike of the faults within a fractured medium. In this study we scrutinize this hypothesis using synthetic data from numerical models.

Numerical modelling provides full control over experiments and implementation of parameters and allows us to understand in a controlled environment the interaction of Rayleigh waves with faults. We model synthetic surface waves that can then propagate through media of our choosing, that is, different geological scenarios with varying degrees of anisotropy. Furthermore, the array design can be altered to determine an ideal way to deploy seismometers for ambient noise studies.

This study addresses the following research questions: First, if the fast direction corresponds to the orientation of a fault, and what effect different geological settings have on Rayleigh wave anisotropy observed with 3C beamforming. Second, if all arrays retrieve this fast direction equally well,

answering the question: What is the ideal array design that does not bias the observed anisotropy? In the next section we introduce the numerical modelling scheme, the geological scenarios considered, and the beamforming method. This is followed by a presentation of the beamforming results of the synthetic datasets considering different models as well as different receiver and source layouts. We conclude with a discussion and a summary of our main findings, highlighting the improved understanding of Rayleigh wave behaviour in fractured media, fast directions in relation to fractures, understanding the importance of modelling parameters and applications for geothermal field characterization.

2. Methods

2.1. Rotated Staggered Grid - Finite Difference Scheme

The first step of our workflow (Fig. 1) comprises numerical wavefield modelling. In this study, a Rotated Staggered Grid (RSG) - Finite Difference (FD) scheme [21] is used to simulate the full elastic 3D wavefield through the different models. The RSG-FD was used for its excellent capability at handling heterogeneous models with stark contrasts, for instance, when fractures are implemented. Furthermore, the RSG FD has been proven accurate when modelling Rayleigh waves [22]. Anisotropy was introduced through changes in elastic properties according to the fault geometries and properties.

The model size was selected to enable simulations with similar sizes and frequencies. Initial simulations of a homogeneous medium were assessed to ensure that the models were numerically stable and had no numerical dispersion; this provided the optimum grid spacing, number of grid points and fundamental frequency (f_{fund}) used for all other models. Simulations were three-dimensional (3D) to implement different fault strikes. Each model has a free surface at the top of the model with the parameters of a vacuum (as this is how the RSG-FD implements a free surface) where surface waves are created (retrograde and prograde Rayleigh waves). A grid size of 150 x 300 x 300 grid points was used, equal to 1.5 x 3 x 3 km (depth x N-S x E-W), with a grid spacing of 10 m. When designing the models, two main simulation criteria had to be considered: stability (von Neumann stability) and dispersion criterion [21]. Runtimes are, on average, approximately 1 hour and 18 minutes per simulation ($\pm 20 minutes$), with 3 nodes and 23 tasks per node for each simulation on the a high-performance computing (HPC) cluster.

To prevent boundary reflections from interfering with surface waves, absorbing boundary conditions were applied to the sides and bottom of the model. A point source with a Ricker wavelet and a fundamental frequency of $f_{fund} = 3Hz$ was used for all simulations. Key model parameters were edited for the models: P-wave velocity (V_P), S-wave velocity (V_S) and density (ρ). Rayleigh wave velocities (V_R) can be estimated using $V_R = 0.9 \times V_S$. Once V_R is calculated, the expected wavelengths (λ) of the Rayleigh wave can be deduced using frequency, $\lambda = V_R/f_{fund}$ (maximum wavelength, $\lambda_{max} = V_{Rmax}/f_{fund}$ and minimum wavelength, $\lambda_{min} = V_{Rmin}/f_{fund}$). λ_{max} and λ_{min} are required to derive the optimal receiver spacing for beamforming, as we will explain in section 2.2.

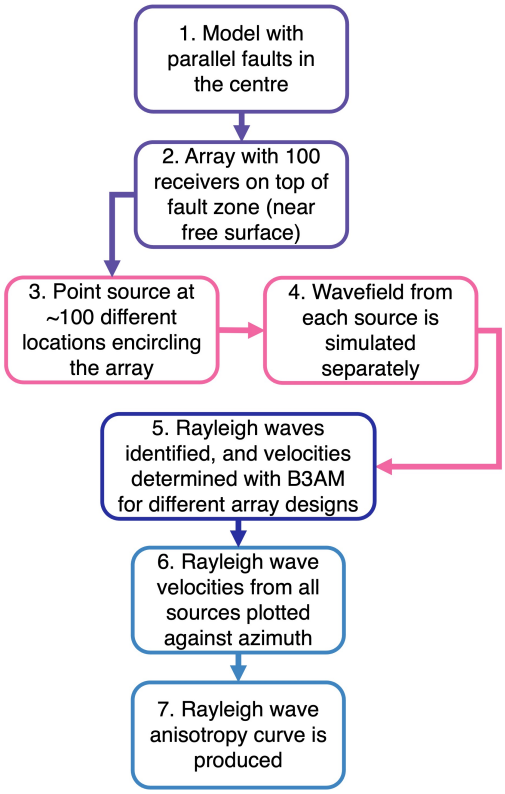

Figure 1: Workflow of methodology, this workflow was applied to both conceptual models of fractured media (with and without faults).

A conceptual model with a homogeneous half-space was used for each medium in the simulations. Anisotropy was applied as five faults, 40 m in

width (including "damage zone", 10 m on each side, around each one) and the full length of the model (no variation with depth), and 100 m apart, as fractures tend to be in multiples and parallel to each other based on stress orientations. Velocities and densities used to implement these conditions are shown in Table.1. For the conceptual models, values from two different examples of fractured media were used. These case studies were two geothermal field locations (Section.2.1.1) and values for both the surrounding rock and fault-"fill" were decided based on literature for the two areas and known parameters of rocks [23; 24; 25; 26; 27; 28].

Geological Scenarios	**Surrounding rock**			**Fault "fill"**		
	V_p	V_s	ρ	V_p	V_s	ρ
Cornwall, UK	4800	3000	2640	1100	630	1760
LHGF, Mexico	4500	2700	2565	2400	1357	2039

Table 1: Parameters for the two geological scenarios used within the conceptual models, showing the compressional velocity (V_p), shear velocity (V_s), V_p/V_s ratio of 1.6 to 1.77 and density (ρ) of both the surrounding rock and the "fill" of the fault. V_p and V_s in ms^{-1}, and ρ in kgm^{-3}.

Rayleigh wave velocities are between 567 ms^{-1} and 2700 ms^{-1}, and the expected wavelengths ($\lambda = v/f$) are in the range of 189 m to 900 m.

Ambient noise was difficult to replicate within a given simulation due to the aforementioned computational expense of a large model, therefore limiting source combinations. Alternatively, transient Rayleigh waves were simulated from a single, moving point source at 0.4 km depth for the purpose of surface waves anisotropy analysis. Its lateral position changed from $270° = South$ (with a backazimuth of $-90°$ relative to the receiver array) moving counterclockwise towards $0° = East$ and finally at $90° = North$ azimuth to enable Rayleigh waves from different directions to interact with the faults.

Producing an isolated Rayleigh wave in a 3D model is challenging, as a large distance between source and receiver(s) is required for body and surface waves to separate, resulting in a large model and, hence, high computational costs. Instead, the distance between the source and receiver array was chosen to be large enough for the wavefront to arrive at the receivers as a plane wave as required when applying beamforming. 1.5 km was determined empirically to be a sufficient distance between source and receiver array for the considered wavelengths.

The fault width-to-wavelength ratio will affect the behaviour of Rayleigh waves when encountering a fault. If the ratio between the fault and wave-

length is too small, smaller waves will get trapped inside faults and cause reflections. The preferred ratio used was 1:10, which is based on the real-life fault width-to-wavelength ratio in the Los Humeros study area. Although slightly higher frequencies are used for the conceptual models than real-world examples, the ratios are kept the same.

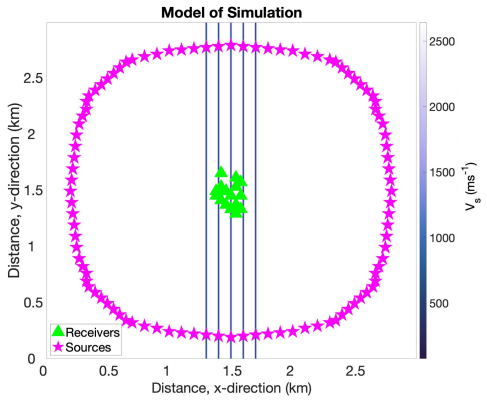

Figure 2: Source and receivers layout, with five parallel faults ($\theta = 0°$), 40 m width each and 100 m apart, with sources at all azimuths, for a conceptual model of Los Humeros, showing all source locations used. A circular source layout was used to get sources interacting with the faults at full coverage of different angles.

2.1.1. Case Studies for Numerical Models

Conceptual models based on geological parameters from two geothermal sites were used to assess Rayleigh wave behaviour in a fractured medium. Los Humeros Geothermal Field (LHGF) in Mexico, and undergoing geothermal reservoir developments in Cornwall in England, UK, mainly based at the geothermal reservoir at Eden Geothermal site [29].

The LHGF in Mexico is situated in the Los Humeros Volcanic Complex (LHVC) in the eastern part of the Trans-Mexican Volcanic Belt [30] and was the area of focus in a previous study [6]. It has been used for geothermal exploration for many decades [31] and is in an extremely complicated geological area with an active tectonic fault system [3]. There are two main calderas and resurgence faults, which are the main source of secondary permeability for the transportation of hydrothermal fluid flow through the reservoir to be then pumped up to the surface for electricity production [3]. Seismic anisotropy investigation was conducted to understand how deeply these faults permeated into the subsurface [6]. One main rock type observed within the region

is andesitic lavas, formed from a variety of explosive and effusive eruptions throughout the region's history, whilst the resurgence faults are found to have quartzite/sandstone deposits due to retrograde mineralisation caused by hydrothermal alteration [23; 32]. The andesitic rock with quartzite faults is the main focus of this study, which is to recreate a simplified LHGF in a numerical simulation to compare synthetic anisotropy results to previously acquired anisotropy, providing a fuller understanding of how Rayleigh wave velocities interact with the faults in this geothermal field.

Cornwall is situated in the southwest of the UK. It is dominated by a large granite intrusion and, due to its radiogenic granite outcrops, has the highest geothermal heat flow in the UK [33]. Several studies have shown the heat flow using borehole data, showing temperatures of $200°C$ at 5 km depth [34]. Geophysical studies have been conducted on the extent of the granite, including gravity surveys that show negative Bouguer anomalies associated with granite [33]. They suggest that the exposed granites are cupolas (an upward protrusion from the roof of a large igneous intrusion [35]) on a single elongated batholith, called the Cornubian batholith, which reaches a depth of at least 8 km, potentially 20 km [33]. The St Austell granite, a large granite pluton protruding from the Cornubian Batholith, is surrounded by metasediments and metamorphosed country rock due to the intrusion event of the granite [36]. The granite, specifically the St Austell pluton, has faults/fractures throughout, which tend to be filled with clay [26; 37; 38]. This extensively clay-filled fractured granite is numerically modelled to assess the differences in Rayleigh wave anisotropy for a geologically differing geothermal reservoir. As St Austell granite in Cornwall, is a fractured medium different from Los Humeros, parameters based on geology were used in a conceptual model to look at how drastically different parameters can affect Rayleigh wave propagation (Table.1).

2.2. Beamforming

Single-component (1C), vertical, beamforming is a commonly employed array processing technique for estimating the azimuth and slowness of the seismic waves arriving at an array [39; 40]. It uses the differential travel times of the plane wavefront due to a specific slowness and back azimuth to individual array stations. If the single-station recordings are appropriately shifted in time for a certain back azimuth and slowness, all signals with the matching back azimuth and slowness will sum constructively [19].

Three-component (3C) beamforming, similar to 1C beamforming, can extract the azimuths and phase velocities of coherent waves in a finite time window. Additionally, it can decompose polarization of the wave from the energy distribution among the vertical and horizontal components of the sensors, enabling the differentiation of the different wave types such as Rayleigh and Love waves [1; 20].

Beamforming is often used for ambient noise wavefields [1; 40; 41], although it was originally used for earthquake analysis [19]. This is because ambient noise provides a large degree of source coverage from several locations, which creates significant surface wave energy that is widely available even when seismicity is typically low [1]. However, beamforming can also be used for transient signals from a single location, such as earthquakes, which may be useful when known point sources are the desired sources for analysis. Note, however, that a general assumption is that waves arriving at the array are planar. Thus, the analysis of seismicity close to the receiver network require different methods.

B3Am, a beamforming toolbox for 3-component ambient noise [18], is the 3C beamforming method used in this study. This study focuses on the analysis of retrograde Rayleigh waves, which typically constitute the fundamental mode and are often the dominant component in the ambient noise wavefield. Rayleigh waves are described as an ellipse in the vertical-radial plane [1]. There are two different types of Rayleigh waves, prograde and retrograde, with different particle motions: prograde Rayleigh wave's elliptical motion is parallel relative to the direction of propagation [42], whilst retrograde Rayleigh waves are anti-parallel [43].

When ambient noise is analysed, beamforming is applied to one time window of noise recording at a time. The window length is typically determined by the largest period in the signal [1; 20]. For the synthetic data in this study the time windows need to be adjusted so that one Rayleigh wave will arrive within one-time window rather than several, based on the time it takes for the waves to traverse the maximum aperture of the varying arrays. Time windows overlapped each other by 75%.

2.3. Anisotropy Analysis

Anisotropic velocities in low-frequency Rayleigh waves could indicate faults continuing at depth within a fractured media. Fig.3 shows the variation in velocity of passive seismic data from the Los Humeros Geothermal Field in Mexico. The surface waves identified in the ambient noise wavefield

were analysed at discrete frequencies and in short time windows individually and combined into a histogram (Fig.3) [6].

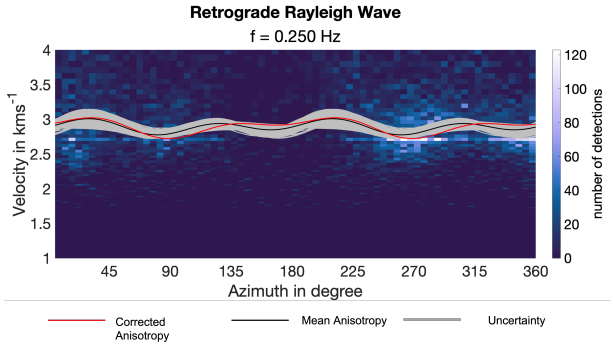

Figure 3: Histogram showing the change in velocity as a function of azimuth in the form of the anisotropy curve of a Retrograde Rayleigh wave of a frequency of 0.25 Hz. A number of detections (colour bar), anisotropy corrected for the array effect (red line), mean anisotropy (black line), the uncertainty of mean anisotropy (a grey area) [6].

In Kennedy et al. [6], anisotropy parameters (for Fig.3 they we were $a_0 = 2.8924$, $a_1 = 0.0476$, $a_2 = 0.0167$, $a_3 = -0.0522$ and $a_4 = 0.0594$) from a Matlab fitting function (Equation 1) were fitted to the velocity versus azimuth histograms for both Love and Rayleigh waves (originally defined by Smith and Dahlen [44]).

$$v(\theta) = a_0 + a_1 cos(2\theta) + a_2 sin(2\theta) + a_3 cos(4\theta) + a_4 sin(4\theta), \qquad (1)$$

where θ is the direction of propagation, measured anti-clockwise from the east, v is the phase velocity in kilometres per second (km^{-1}), and a_i are the anisotropy parameters. From the anisotropy curve we obtain the azimuth of the fast direction (here 35 and 210°). Fast directions of anisotropy have been linked to fault strikes when looking at anisotropic models [7], which denotes this important relation between fast direction and structural anisotropy. We will investigate in detail in this study how this is related to the strike of the fault.

A maximum response for each time window of the data was chosen, and all the velocity-azimuth pairs were plotted into the histogram, which provides information about the number of detections from the ambient noise wavefield and the anisotropy curve was fitted to the data to describe the velocity and azimuth variation [20]. We will not use such a histogram for the synthetic experiment but one velocity azimuth pair for each source location.

2.4. Array Design

The velocities and azimuths detected with B3Am can be influenced by array effects [45] The observed anisotropy can therefore be biased by so-called apparent anisotropy, which results from an anisotropic distribution of stations, for example [46; 6]. To account for the array effects, it is beneficial to reduce any apparent anisotropy, the underlying anisotropy caused by the array itself (array response functions can also be used to monitor the array effect).

To account for the apparent anisotropy, conceptual models and homogeneous models, with no anisotropy applied, were simulated through numerical modelling. This enabled the analysis solely of the array's effect on the synthetic data.

An ongoing debate in the ambient noise community is the best array design for the optimum ambient noise studies [47; 45; 48]. Tests have been done in the past [49; 45; 50] to check this as well as accounting for array effects on azimuth. Studies suggest that the best array designs are those without a preferential direction, for example, triangular, circular, or random arrays [47; 45]. Varying the number of receivers changes the wavenumber range the array is sensitive to in the beamformer analysis. In this study, four main receiver layouts were tested (Fig.4): rectangular, random, circular and GEMex (the seismic array deployed in Los Humeros, Mexico, for the GEMex project, used in [41; 6]). A 100-receiver array was implemented to collect synthetic data, which enabled specific receivers to be selected afterwards and to realise different array layouts and receiver spacings; receiver locations were restricted by the 100-station array. This means that a simulation for a chosen model would only need to be run once rather than repeatedly for the different array designs. Two different types of fractured media were tested with these different arrays. Furthermore, the two different media were modelled without faults to assess the effect of the array alone.

One key component in array design is the receiver spacing, the two most important values being the minimum, d_{min} and maximum d_{max} receiver spacing. Whilst the array design was modified, the overall rules for the array spacing are based on two equations, which denote the d_{min} and d_{max} allowed in order to perform beamforming analysis of a data set, as only certain wavelengths (λ) will be resolvable by the array. Based on recommendations by Tokimatsu et al. [51] for array design.

$$\lambda_{max} < 3d_{max} \tag{2}$$

$$\lambda_{min} > 2d_{min} \tag{3}$$

All arrays had $d_{min} = 40m$, whilst d_{max} varied between 320 and $394m$ (all apertures are within conditions recommended in Equations 2 and 3. We used 17 receivers in each array (16 in the case of the rectangular array) to allow for the direct comparison to real data results from [6], where a maximum of 17 receivers was used for optimum data coverage.

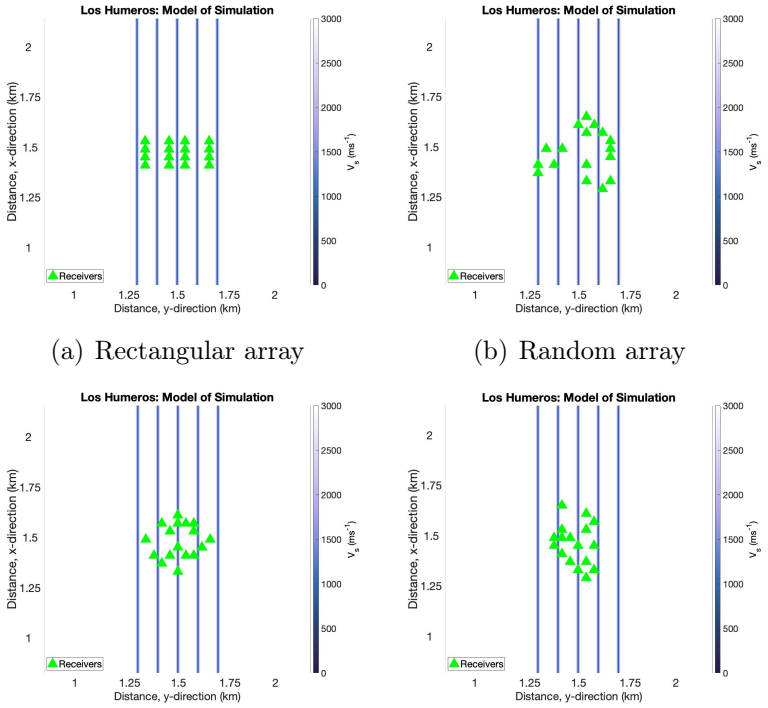

(a) Rectangular array (b) Random array

(c) Circular array (d) Gemex array

Figure 4: Array designs with five parallel 40 m faults for the conceptual model of Los Humeros, using 17 receivers (16 for (a)), for (a) Rectangular array $d_{max} = 342m$, (b) Random array $d_{max} = 394m$, (c) Circular array $d_{max} = 320m$ and (d) Gemex array $d_{max} = 379m$.

2.4.1. Varying V_P/V_S ratio and Density

P waves have vertical motion, whereas S waves have both horizontal and vertical motion (SH and SV) [52; 53]. Rayleigh waves include both vertical and horizontal components of P-SV waves [54]. Typically, when estimating the Rayleigh wave velocity range for the simulations, only V_S was considered.

Rayleigh wave velocity is said to be $V_R = 0.9 \times V_S$, where V_P is ignored [55]. However, the Rayleigh wave velocity ratio with regard to V_P and V_S has been shown to vary depending on the Poisson's ratio [56]. The dynamic Poisson's ratio (V_d) has a direct relation with V_P and V_S and can be determined by the following relationship [57; 58; 59],

$$V_d = \frac{\frac{1}{2}(V_P/V_S)^2 - 1}{(V_P/V_S)^2 - 1} \tag{4}$$

As V_d varies due to V_P and V_S, the Rayleigh wave velocity also varies [56], due to V_P and V_S relation with Poisson's ratio and Rayleigh wave velocity. This illustrates the ratio between the value of V_P and V_S can have an impact on the Rayleigh wave velocity. Fractured media in geology have various V_P/V_S ratios of different rock types, and they vary depending on various conditions exerted on the rocks (such as stress or fluid content) [60]. To assess how different V_P/V_S ratios may affect interpretations of retrograde Rayleigh wave velocities obtained from B3Am, a simulation was done using a source at $azimuth = 0$, constant ρ and V_S as in the Cornwall scenario (rock only, no fault), and a varying V_P to change V_P/V_S ratios from ratio from 1.55 to 1.85, increasing by 0.05, (which is a reasonable range of V_P/V_S ratios [61]). Fig.5 shows that the Rayleigh wave velocity does vary with the V_P/V_S ratio as suspected based on Achenbach [56]. Therefore, the V_P/V_S ratios for the simulations were maintained within a small range for the different parameters for the fractured media to reduce any additional changing constants.

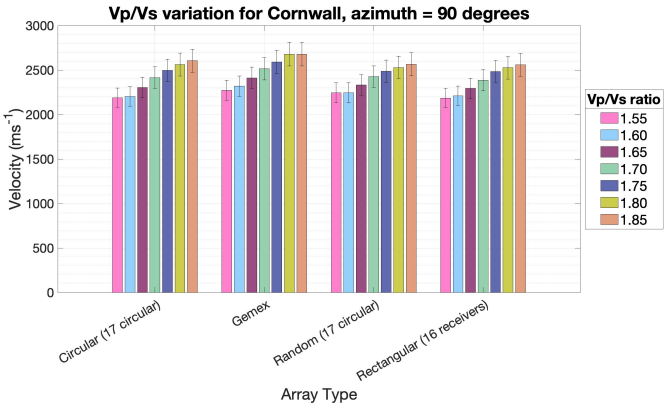

Figure 5: Velocity variation for different Vp/Vs ratios, changing the Vp parameter, with a homogeneous model for conceptual model of Cornwall with a source of azimuth = 0°

A similar study was carried out to assess the influence of the density on estimated Rayleigh wave velocities. The effect is negligible, and results can be found in Appendix A.

Our findings from V_P/V_S ratio and density variation show how the beamformer perceives the Rayleigh wave velocity changes from these conceptual models of fractured media. However, real data Rayleigh wave velocities may not behave the same way when there is a V_P/V_S ratio and density variation.

3. Results

3.1. P and Rayleigh wave arrivals

Fig.6 shows some examples of the time series from 16 receivers in a rectangular array, where the wavefield is coming from $270° = South$ for the Los Humeros model with faults. Fig.6a shows the z component (vertical, depth) amplitude, Fig.6b is the y component (horizontal, N-S) amplitude. The two black lines depict the beamforming time window where the P wave arrives, which we can recognise in the time series due to the smaller vertical amplitude in Fig.6a and the higher amplitude in Fig.6b, which corresponds to the P wave motion excited by a shallow source. Fig.6c is the beam power response plot, where the top plot shows the maximum beam energy response for the wavefield in the time window indicated in a and b. The maximum value in this plot corresponds to the wavenumber-azimuth pair that fits the observed wavefield best in this time window (shown by red intersection); the wave type in the bottom plot corresponding to this point is the dominant wave type arriving at this time window. In Fig.6c, this is the P wave. Comparably, in Fig.7 in a later time window, we see evidence of the retrograde Rayleigh wave, shown by the high amplitude for the vertical component (7a), smaller amplitude in the horizontal (7b) and dominant wave type shown as Retrograde Rayleigh arriving from the correct source direction of $270° = South$ (7c). Thus, the particle motion of the Rayleigh wave describes a vertically polarised ellipse, as we would expect for a mostly homogeneous medium without a sharp velocity contrast at depth and a Poisson ratio close to 0.25 [56].

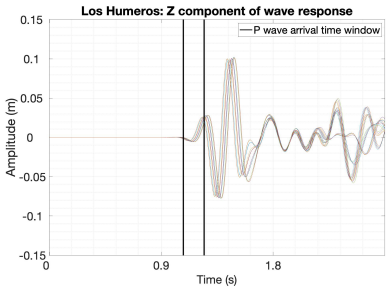

(a) Times series of Z component

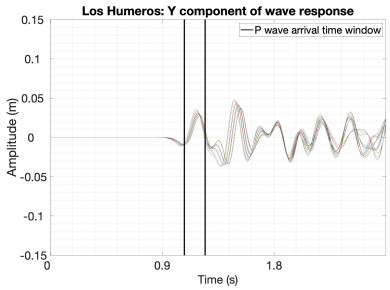

(b) Times series of Y component

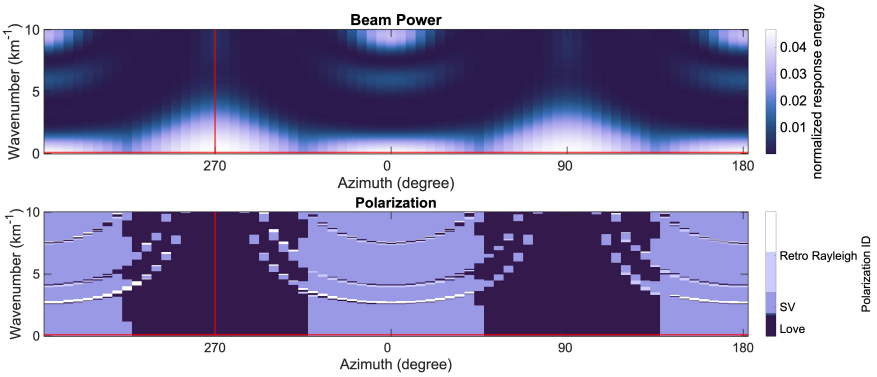

(c) Beam power plot

Figure 6: Seismic traces and beam power plot for (a) times series in z-direction (depth) with P wave arrival highlighted, (b) times series in y-direction (N-S) with P wave arrival highlighted (c) Beam power plot depicting the P arriving from the 270° = *South*, shown by red intersection point (twin = 6, $t = 0.71$ to $0.83s$). This is for a rectangular array with 16 receivers for the conceptual model of Los Humeros with faults.

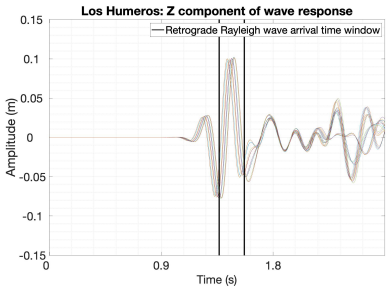

(a) Times series of Z component

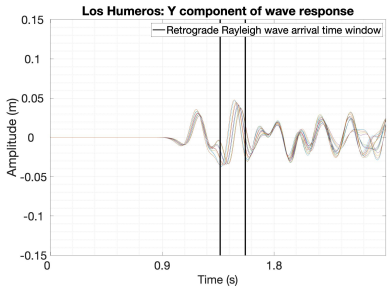

(b) Times series of Y component

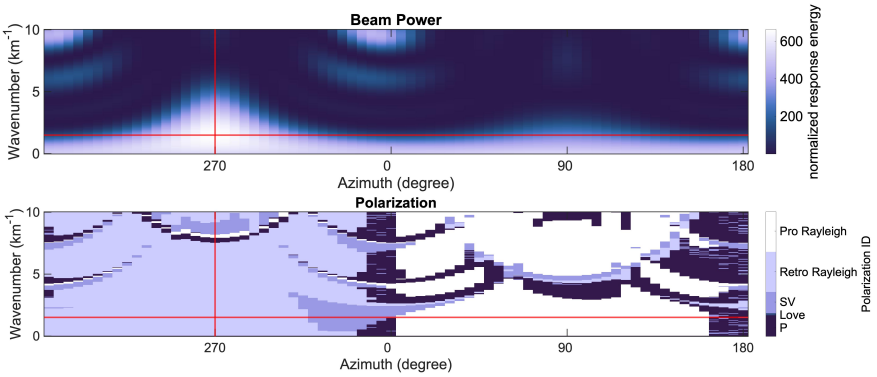

(c) Beam power plot

Figure 7: Seismic traces and beam power plot for (a) times series in z-direction (depth) with retrograde Rayleigh wave depicted, (b) times series in y-direction (N-S) with retrograde Rayleigh wave arrival depicted $t = 1.54$ to $1.65s$, (c) Beam power plot depicting the retrograde Rayleigh wave arriving from the $270° = South$, shown by red intersection point (twin = 13, $t = 1.54$ to $1.65s$). This is for a rectangular array with 16 receivers for the conceptual model of Los Humeros with faults.

The P wave and retrograde Rayleigh wave, in Fig.6 and Fig.7 are arriving from $270° = South$ due to the source position in these examples. As the source is moved, it will interact with the fault and arrive at the array at different angles, altering the velocity and azimuth of the identifiable Rayleigh wave and enabling anisotropy analysis.

Fig.8 shows examples of three-dimensional (3D) and two-dimensional (2D) snapshots for the conceptual model using parameters from Cornwall, at $t = 1.58s$ (within the time window where Rayleigh waves are depicted to arrive) of the synthetic waves propagating outwards from the source location ($270° = South$) through the model. Fig.8a and c represent a model without faults, whilst Fig.8b and d represent a model with faults.

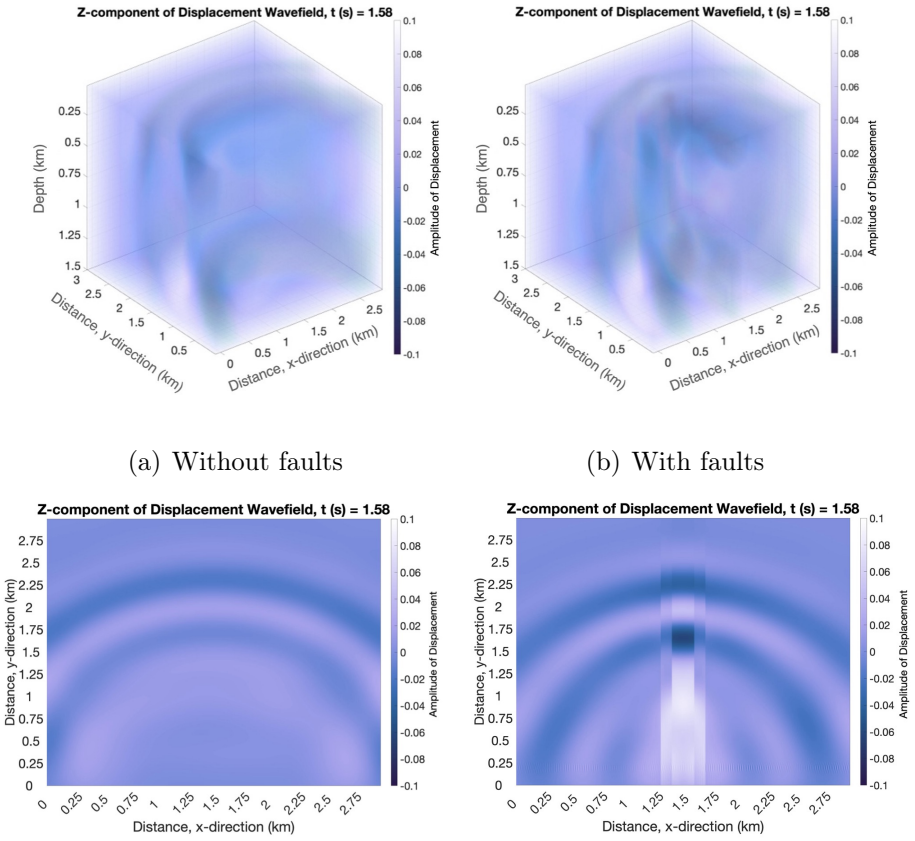

(a) Without faults

(b) With faults

(c) 2D Top-down view: Without faults

(d) 2D Top-down view: With faults

Figure 8: 3D and 2D snapshots at $t = 1.58s$ of retrograde Rayleigh wave propagating through a model for a conceptual model of Cornwall from source location $270° = South$, (a) 3D view without faults, (b) 3D view with faults, (c) 2D, top-down view, without faults and (d) 2D, top-down view, with faults. The colour bar represents the amplitude of displacement of the wave.

3.2. Wave Type Identification

B3Am was used on every synthetic dataset to identify a retrograde Rayleigh wave for velocity analysis. Similar to Fig.7(c), beam power plots were produced for all array types to assess whether retrograde Rayleigh waves could be identified in the wavefield. For a retrograde Rayleigh wave to be positively identified, it would need to arrive in a time window (± 1 time window) after a P wave and with the azimuth of the source direction so that it is certain that the wave is a direct wave. All beam power plots for the different arrays

(rectangular, random, circular and GEMex) showed an identifiable retrograde Rayleigh wave, mostly in time window $= 13, t = 1.54$ to $1.65s$ (examples can be seen in Fig.A.16 in Appendix A). All beam power plot examples are for the conceptual model of Los Humeros. Similar analyses were also conducted on conceptual models of Cornwall so that the differences in Rayleigh wave anisotropy depending on geologically different fractured media could be assessed. We observe some instances where the propagation direction of the Rayleigh wave, if it hits the fault under a small angle ($\simeq 20°$), gets aligned with the fault.

We estimate Rayleigh wave velocity as a function of azimuth by placing sources in different directions with respect to the array and the faults. Fig.9 shows beampower plots from correctly identified Rayleigh waves from different directions. In Fig.9a, we see a clear retrograde Rayleigh wave coming from the South, which correlates correctly to the source location. Fig.9b is also a direct retrograde Rayleigh wave, in this case coming from the East ($0° = East$), which matches the source direction used for this simulation.

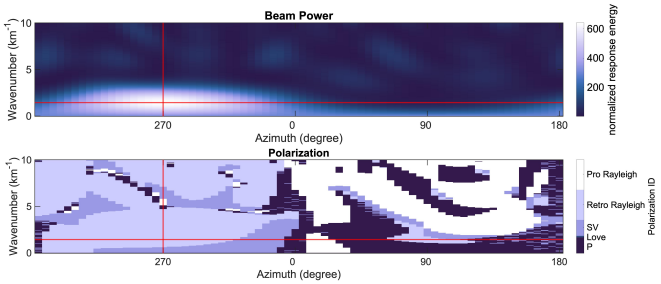

(a) Source from the South

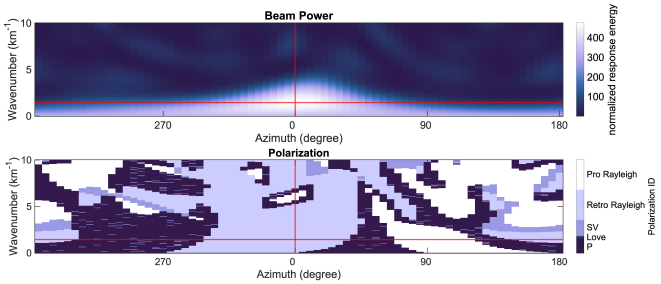

(b) Source from the East

Figure 9: Beampower plots for a conceptual model of Los Humeros with faults, from the GEMex array, for two different source locations, (a) twin = 13 (1.54 to 1.65s), 270° = *South* on the x-axis and (b) twin = 13, 0° = *East* on the x-axis (East).

3.3. Anisotropy

The velocity for each identified retrograde Rayleigh wave was calculated using the corresponding wavenumber, k (picked at the point of the maximum beam energy response (red intersection point)), and $f_{fund} = 3Hz$ (we looked at beam power results for f = 3 Hz which is the fundamental frequency of the model) using $v = f_{fund}/k$. These velocities were then visualised in azimuth vs velocity plots for all array designs (Fig.10), for both conceptual models.

Fig.10(a) shows the azimuth-dependent Rayleigh wave velocities for the Los Humeros model for the four different arrays. Velocity picks and the corresponding fitted curve for each individual array are provided in the Appendix (Fig.A.18). The strike of the fault is indicated by a solid vertical line at an azimuth of 90° (270°; plots are symmetric around 180° and here and in the following, values in parentheses denote the equivalent azimuth +180°).

Overall, the anisotropy for the conceptual model of Los Humeros depicts a 4θ anisotropy response for all arrays, though less pronounced for the random array (yellow curve). 4θ anisotropy, first demonstrated by Backus [62]

using perturbation theory, refers to the general form of the azimuthal dependence of the phase velocity of horizontally propagating P wave, which is a homogeneous trigonometric polynomial of degree 4 in θ, where θ is the azimuth of the horizontal wave vector [44] and is related to 90° symmetry [63]. This was then related to the azimuthal dependence of Rayleigh wave phase velocity by accounting for Rayleigh's principle by Smith and Dahlen [44]. This is written as a Fourier series in θ with five anisotropy coefficient [44], shown in Equation.1.

The fastest velocities are observed around 60° (240°) for all but the random array, deviating significantly (by up to 40°) from the fault strike; similarly for the secondary peak at around 125° (305°). For the random array, we observe a fast direction at $\simeq$ 80° close to the true fault strike and no pronounced secondary peak in the anisotropy curve.

The slowest velocities (troughs) occur around $0 - 20°$ $(180 - 200°)$ for all arrays, that is, close to the direction perpendicular to the fault. Local minima in the curves derived from the circular and the GEMex array coincide with the direction parallel to the fault at 90° (270°).

The magnitude of anisotropy (a_{mag}) varies between around 2.4% measured with the rectangular array and 7.3% for the GEMex array (all anisotropy parameters can be seen Table.A.2).

Fig.10(b) provides the azimuth-dependent Rayleigh wave velocities for the Cornwall model, granite with clay-filled faults. The periodic velocity pattern exhibits 4θ anisotropy, with large velocity variations. Fig.10(b) shows the fast directions (peaks) are parallel to the fault strike at azimuth 90° (270°) and the slow directions (troughs) are at azimuths 45° (225°) and 150° (330°).

The slowest velocities at azimuths of 330° and 150° are within a range of ±30° from 0° (or 360°) and 180° azimuth (perpendicular to faults), with increases to the maximum velocities at the parallel azimuths (90° and 270°) respectively. Differences in velocity depending on array design are minimal, with the random array providing overall slower velocities. Importantly, the fastest velocities for the Cornwall model are measured parallel to the faults. The magnitude of anisotropy (a_{mag}) varies between around 21.3% measured with the random array and 28.3% for the circular array (all anisotropy parameters can be seen Table.A.3).

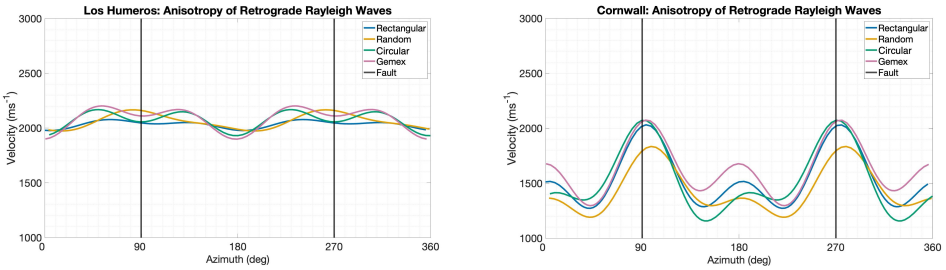

(a) Model of Los Humeros (b) Model of Cornwall

Figure 10: Azimuth of source vs velocity plots for Retrograde Rayleigh waves for all array designs, for (a) conceptual model of Los Humeros, a_{mag} range of 2.4 to 7.3 % and (b) conceptual model of Cornwall, a_{mag} range of 21.3 to 28.3 %. Azimuth steps are 2.3°, 270° is parallel to faults, and 0° is perpendicular to faults. Black lines depict the fault strike, and anisotropy curves are fitted to data picks using the fitting function (data picks shown in Fig.A.18).

Simulations for both scenarios for all azimuths were made on models without faults present (shown in Fig.11). Fig.11(a) shows the apparent anisotropy. These tests were done to assess the effect of the array design. Fig.11(a) shows that the fastest velocities are at 130° and 360°, with the slowest velocities at 90°. The overall velocity range is small or smaller than the examples with faults, $400ms^{-1}$, and the fastest velocity ($2450ms^{-1}$) is slightly faster than the expected isotropic velocity (around $V_R = 0.9 \times V_S$) at $2430ms^{-1}$.

Differences between anisotropy for different array designs also indicate a minimal array effect. Additionally, the peaks and troughs differ from those observed in the heterogenous models for Los Humeros, confirming that these are indeed caused by the presence of a fault. Cornwall has a much smaller anisotropic response from the homogeneous simulations (Fig.11(b)). In this example, there is a relatively constant velocity of $2300 \pm 100ms^{-1}$, which is slower than the expected isotropic velocity of $2700ms^{-1}$ but is inside the expected uncertainty range. Furthermore, the apparent anisotropy has minor velocity variations, with the largest differences being caused by rectangular arrays, showing that rectangular arrays are the least ideal for anisotropy analysis. However, the lack of difference in anisotropy pattern is noteworthy for the different array types, when more variation would be anticipated, this is discussed further in Section.4.1.

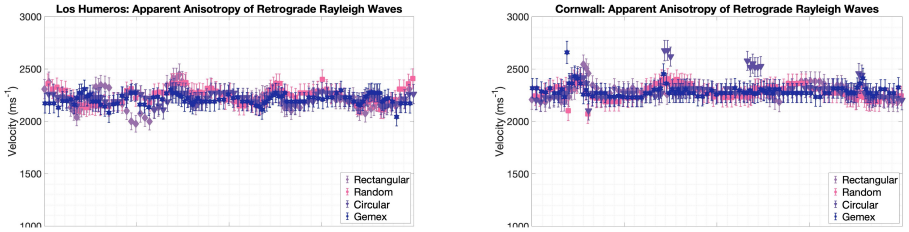

(a) Model of Los Humeros (b) Model of Cornwall

Figure 11: Apparent anisotropy for Retrograde Rayleigh waves for all array designs, for (a) conceptual model of Los Humeros and (b) conceptual model of Cornwall. Azimuth steps are $\simeq 2.3°$.

3.3.1. Importance of Source location

Throughout various ambient seismic studies [47; 45; 48], the receiver layout is always treated with a degree of care to obtain optimal results, whereas the source layout tends to be not considered to the same degree. However, the source layout is frequently analysed in interferometric approaches where isotropic noise sources are needed to calculate stable and unbiased Green's functions [64]. Often beamforming is used to estimate to estimate the homogeneity of the noise wavefield with respect to azimuths [64]. The anisotropy curves for the different source locations can be seen in Fig.12.

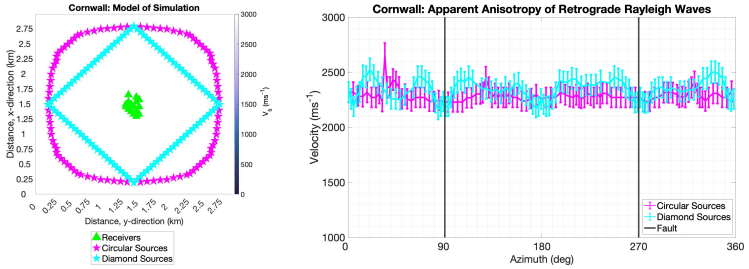

(a) Model (b) Cornwall, GEMex array: Anisotropy curve

Figure 12: Apparent anisotropy for Retrograde Rayleigh waves for the GEMex array design with the diamond vs circulars distribution for Cornwall without faults (a) Model of two different source layouts, for (b) Anisotropy curves for GEMex array with different source layouts. Azimuth steps are $\simeq 2.3°$.

Using a diamond shape instead of a circle, we deliberately vary the source-array distance with azimuth so that Rayleigh waves arrive at the array in

different time windows for different sources. Fig.12 shows that there is more anisotropy variation for the diamond source layout than the relatively constant velocity for the circular source layout (with the exception of 35°).

4. Discussion

We used numerical modelling to generate Rayleigh waves in faulted models and performed anisotropy analysis on synthetic array data using three-component beamforming. There are clear variations in observed anisotropy, depending on how anisotropy is implemented by moving a source relative to the fault depending on model parameters (e.g., V_S) as well as acquisition parameters (source/array layout). The main observations are that the array design has only a minor impact on the observed anisotropy while the geology, such as the difference in V_S for the different scenarios, greatly impacts the anisotropy response.

4.1. True vs Measured Azimuth

The azimuth obtained from the beamformer could be slightly influenced by the faults and source azimuth. Fig.10, Fig.11 and Fig.12(b) all refer to the velocity vs known azimuth of the various scenarios that they depict. The known azimuth is the azimuth calculated based on the known source location, instead of the measured azimuth as extracted from the beamformer. Fig.13 shows the variation of velocity as a function of known and measured azimuth for a conceptual model of Los Humeros with faults using wavefield values from the GEMex array layout. Fig.13 shows that the B3Am extracts azimuths very closely to the known azimuth of the sources, with a deviation in the range of the azimuth grid resolution (5°). The largest degree of azimuth offset is in the fast directions, shifting both further from the strike of the fault at 270°. Even though the difference between known and measured azimuth is small, consideration must be taken when looking at the fast directions, accounting for potential offset of azimuth relative to fault strike when looking at fault strikes in real data.

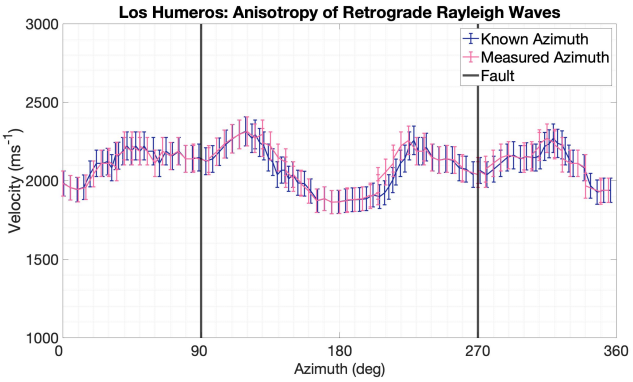

Figure 13: Known Azimuth vs Measured Azimuth of source as a function of velocity for Retrograde Rayleigh waves for GEMex array, for a conceptual model of Los Humeros. 270° is parallel to faults, and 0° is perpendicular to faults (depicted by black lines). Error bars are 5% of the velocity.

4.2. Effects of Acquisition Geometry

Next, let's consider the array effects shown by the beamformer. To focus on the apparent anisotropy effect from different arrays and only arrays with a similar number of stations (17) but different layouts were considered, to not alter too many properties at the same time. Therefore, the 100-receiver array is not used to its full capacity and varying receiver numbers are beyond the scope of this study. A direct comparison between anisotropy with and without faults for the two fractured media is shown in Fig.14, revealing which variation in velocity is related to experimental set-up (i.e., array design and/or source location; see also Section.3.3.1) and which comes from the faults. While the array effect is small, and there is not much variation in the anisotropic response depending on the array shape, it is important to note that for the Los Humeros models the array design slightly affects the fast directions. The array design had a negligible effect on the models of Cornwall. Moreover, between 345° and 15°, some retrograde Rayleigh waves could not be identified within a given time window for some array layouts, indicating that velocities from different arrays that are drastically different must be scrutinised.

Fig.14(a) shows the differences between the homogeneous (without fault) and heterogeneous (with fault) models for the rectangular array. Parallel to the fault (90°) the velocities for both models are similar, which indicates a decrease in the observed velocities (with a fault) at this angle due to the array.

Furthermore, at 60° and 125° and 230°, there would be an increase in the observed velocities with a fault due to the rectangular array. Perpendicular to the fault (180°), there is a slight decrease in velocity for the homogeneous model, which will decrease the observed velocity at this azimuth for the heterogeneous model slightly. This would impact the interpretation of the fault strike from this anisotropy pattern.

Fig.14(b) has a larger difference between the homogeneous and heterogeneous models for the rectangular array. Parallel and perpendicular to the fault, there is a relatively constant velocity for the homogeneous model, which would not cause a change in the observed anisotropy pattern for the heterogeneous model. At 55° there is an increase in velocity for the homogeneous model, which would cause an increase in observed velocity at this azimuth for the heterogeneous model.

Overall, the most interesting outcome is how similar the results are for the different arrays. This may differ for an ambient noise scenario where the wavefield can be a superposition of multiple waves rather than one wave at a time.

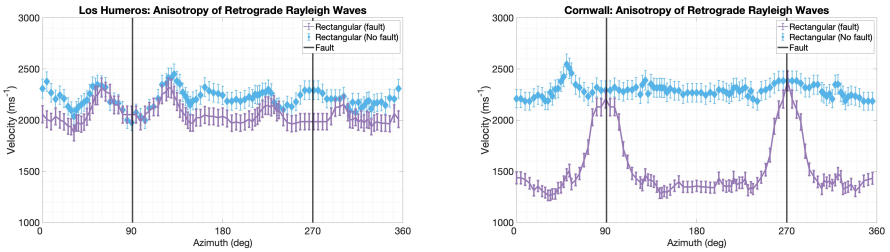

(a) Model of Los Humeros (b) Model of Cornwall

Figure 14: Combined anisotropy for Retrograde Rayleigh waves for all array designs, for (a) the model of Los Humeros and (b) for the model of Cornwall. Azimuth steps are $\simeq 2.3°$.

Fig.12 shows the effect of source layout on Rayleigh wave velocity. Source-array distance affects the separation of wave types. The Rayleigh wave will have separated better from the P-wave when the distance is larger, while the overlap of P and Rayleigh will be more severe for shorter distances. This will influence how well the Rayleigh wave can be recognised by the beamformer and can lead to variations in the estimated velocities and, hence, bias the anisotropy analysis. We point out that this problem arises only when considering transient waves from individual point sources, as in the numerical

model, rather than continuous noise signals. Hence, when Rayleigh waves are extracted from ambient noise and multiple time windows treated statistically (cf. [1]), the effect of the source-array spacing should not play a role. However, when beamforming is to be applied to identify and characterise wave types in transient signals, time window length and overlap can have a significant effect, and results might become more stable when adjacent time windows are analysed jointly. More testing is required to further quantify the behaviour and formulate recommendations for three-component beam response processing and interpretation of transient signals. In real life, however, the source distribution cannot be controlled or known in advance in most ambient noise applications [46].

4.3. Effect of Geological Parameters

We also investigate the effect of the geology (velocity) contrast on the anisotropy. In the case of the model for Los Humeros, there is a smaller velocity contrast between fault fill and surrounding rock (see Table.1), which seems to result in an anisotropy with a more complex pattern (4θ) but which is less pronounced in amplitude. However, for the stronger contrast shown by the model Cornwall, we observe a 4θ anisotropy with an unambiguous fast direction. Fig.10(b) indicates that the Rayleigh waves travelling parallel to the fault are faster. The anisotropy is changed by the presence of the faults, and if the V_S of the surrounding rock and fault-"fill" have a large difference between each other, the anisotropy curve will have higher amplitudes due to dramatic velocity changes.

We assess the point at which the relationship between the velocity of the surrounding rock and fault-"fill" causes a change from 2θ to 4θ anisotropy. Fig.15 shows how the anisotropy response changes from 4θ to 2θ when the difference in velocity for the surrounding rock and fault-"fill" increases ($1357ms^{-1}$ difference in the model for Los Humeros, $2000ms^{-1}$ difference). When the velocity difference between the rock and the fault-"fill" is $1500ms^{-1}$ or less, 4θ anisotropy is observed (expressed by two clear velocity peaks). The dominant slow direction occurs perpendicular to the fault in these cases. For the largest velocity contrast of $2370ms^{-1}$ (Cornwall model) the anisotropy pattern again shows a 4θ periodicity, however, this time we observe two slow directions and one dominant fast direction aligning with the fault strike.

Further, a velocity difference of $2370ms^{-1}$ provides the lowest mean velocity for the anisotropy curve, of $\simeq 1600ms^{-1}$ compared to the model with a velocity difference of $1400ms^{-1}$ which provides the highest mean velocity

of $\simeq 2400ms^{-1}$. Why there is such a dramatic decrease in mean velocity for a velocity difference of $2370ms^{-1}$ compared to the others leaves a question for a future study.

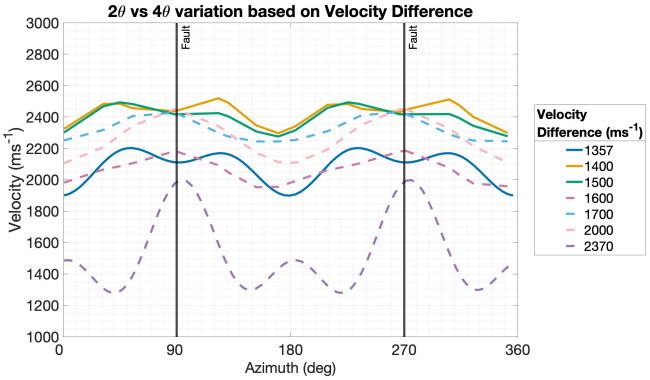

Figure 15: Velocity vs azimuth for a range of velocity differences between the surrounding rock and the fault for GEMex array. Dashed lines depict large velocity differences, and solid lines depict small velocity differences, a_{mag} range of 4.0 to 7.6 % (Table.A.4) Fault strike represented by black lines.

4.4. Observed versus Structural Anisotropy

Regarding the observed anisotropy compared to the structural anisotropy of the conceptual models, the fast direction is well aligned with the fault orientation for the Cornwall model; for the Los Humeros model, it is offset from the fault orientation. The observed anisotropy and structural anisotropy for the model of Cornwall are the same (Fig.10(b)), with the fast directions at azimuths of 90° and 270°. The observed anisotropy for the model of Los Humeros (Fig.10(a)), has fast directions at $30° \pm 20°$ on either side of the structural anisotropy (90° and 270°).

The observed anisotropy and the structural anisotropy fast directions differ for the model of Los Humeros. However, the slow directions may provide a better indication of the fault strike depending on the velocity contrast. The slowest direction for the observed anisotropy is exactly perpendicular to the fault strike for the model of Los Humeros, the model for Los Humeros having a small velcioity contrast between the rock and the faults. Whereas, the model for Cornwall with its high velocity contrast has the fast directions as better indicators of fault strike, with the fast directions parallel to fault strike. This indicates that, in general, the slow directions, as seen by the

beamformer, may be more representative of the structural anisotropy of the subsurface than the fast direction depending on the velocity contrast of the fractured media. Otherwise, the fast direction can sometimes be a better indicator of a fault strike.

4.5. Comparison to Los Humeros Data

Numerical modelling can create a conceptual model to get a complex anisotropy response, similar to patterns seen in real data of fractured media. A previous study [65] underwent full waveform ambient noise inversion using numerical simulations to improve the inversion scheme for tomography. Chaput et al. [66] used numerical analysis to assess the depth sensitivity of Rayleigh waves due to their multi-modal behaviour. However, they found that the numerical models did not explain why the inferred fast directions aligned with the direction of ice flow at high frequencies.

Looking at the results for the GEMex array design for Fig.10(a), to Fig.3 there are similarities in anisotropic curves. However, the numerical results have higher amplitudes (larger velocity fluctuations) than the real data, with both numerical and real results exhibiting the 4θ anisotropy. The higher amplitudes can potentially be reduced by accounting for the apparent anisotropy, although some complexity will remain. This study shows that 4θ anisotropy can result from only one fault orientation (the five faults modelled having the same strike) that exhibits a relatively small velocity contrast with the surrounding rock. The main difference is that we do not assume a perfectly NS striking fault for Los Humeros in the real results, so we can't compare the two plots directly. Numerical results indicate that the slow direction is linked to the fault strike within a fractured medium, indicating the direction perpendicular to the fault strike. Interpreting the data in Fig.3 based on these findings, the slow direction of 90° (North) implies a 0° (East-West) striking fault, which corresponds to the strike of some of the known resurgence faults in Los Humeros [6; 67]).

Numerical models can never be a perfect replica of the real world, but they can provide some useful insights into the degree of complexity we can expect from real data and, therefore, the corresponding anisotropic structure. Furthermore, even relatively simple structures can cause 4θ anisotropy.

4.6. Future: More complex models

Faults vary with depth, and the maximum depth of penetration of the faults can be assessed by observing retrograde Rayleigh waves as a func-

tion of frequency. A depth-dependent numerical model would allow for the observation of this relationship with depth, which requires more computational resources than used in this study. Frequency-dependent analysis, could provide an insight into the variation of anisotropy of a model of fractured media at depth and, consequently, its comparability to real anisotropy data at depth.

5. Conclusions

This study has used numerical modelling to analyse synthetic Rayleigh waves in fractured media, which are identified and characterised using three-component (3C) beamforming of the synthetic wavefield providing anisotropy analysis of surface wave velocities. A previous study [6] hypothesised that the fast direction of Rayleigh wave propagation aligns with the fault strike. However, numerical modelling indicates that this is not always the case. We find that the velocity contrast between fault and surrounding rock controls the complexity and magnitude of the observed anisotropy: a smaller contrast leads to smaller magnitudes but larger complexity/ambiguity (4θ anisotropy), whereas a larger contrast results in larger magnitudes and lower complexity (2θ anisotropy). In the first case, the fast direction could differ by up to 50° from the fault strike. However, slow velocities seem to be aligning with the direction perpendicular to the fault strike when the velocity contrast between rock and fault is small and might, therefore, be a more reliable indicator for fault orientation. In the latter case, the fast direction aligns perfectly with the fault. We further observe variations in the estimated anisotropy depending on the chosen array design. These differences are small when the velocity contrast between fault and surrounding rock is large, however, they become more pronounced for small velocity contrasts and could lead to misinterpretation of the fault strike direction.

6. Acknowledgements

This paper contains work conducted during a PhD study undertaken as part of the Centre for Doctoral Training (CDT) in Geoscience and the Low Carbon Energy Transition, and it is sponsored by the University of Aberdeen via their NERC GeoNetZero CDT Scheme, whose support is gratefully acknowledged. The interpretations and analyses were undertaken in the research facility at the University of Aberdeen, the underpinning financial and

computer support for which is gratefully acknowledged. Furthermore, the modelling was conducted on the HPC Bochum cluster of the chair of reservoir geophysics at Bochum University of Applied Sciences, the use and support of those affiliated with the cluster being gratefully acknowledged.

Appendix A. Supplementary results

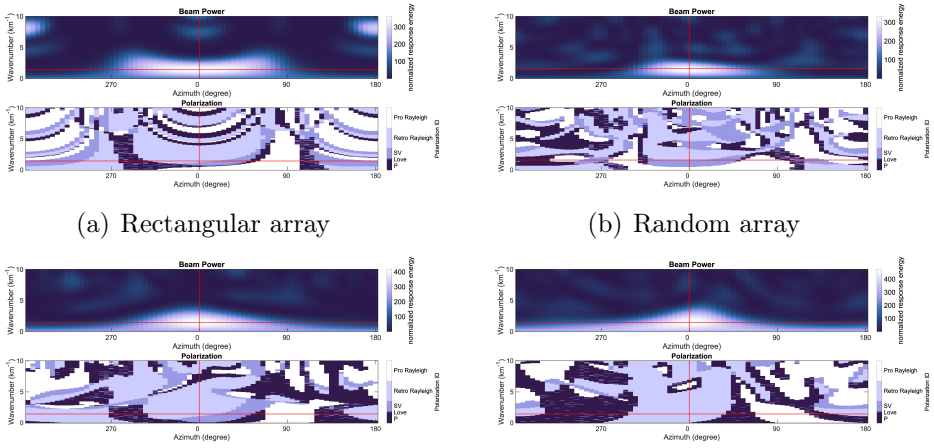

(a) Rectangular array

(b) Random array

(c) circular array

(d) Gemex array

Figure A.16: Beampower plots for three different array designs (17 receivers, 16 for rectangular) for Los Humeros with faults, for the source at $0° = East$ for area (1) without faults. (a) twin = 13 (1.53 to 1.65s), rectangular array, (b) twin = 8, random array, (c) twin = 13, circular array and (d) twin = 13, gemex array. Each plot shows a Retrograde Rayleigh wave as the identifiable wave type in their respective twin's, note that it is normal for the identifiable desired wave type to be within ± 2

Density (ρ) is required to calculate seismic velocities for an elastic media using stiffness tensors. Density varies in different fractured media, and in simulations, it can affect the velocities, but in terms of geological fractured media, the effects tend to be minimal. To assess this the ρ plays a larger role in synthetic Rayleigh velocity than previously assumed simulations similar to those for V_P/V_S ratio, where conducted for a homogeneous model of Cornwall, with a source at $azimuth = 0°$, with constant V_P and V_S, and varying ρ from $2640 kgm^{-3}$ to $2740 kgm^{-3}$, increasing by $20 kgm^{-3}$. Fig.A.17 shows that the density has a negligible effect on the velocity variation for each array type, with there being no difference at all and any velocity changes resulting from

the array design, which is also minimal. Ensuring that, as expected, the ρ has no underlying effects on the Rayleigh wave velocity.

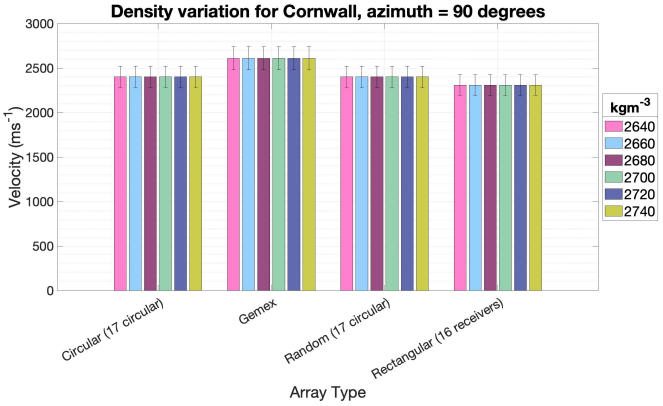

Figure A.17: Velocity variation for different densities of a homogeneous model for conceptual model of Cornwall, with the source of azimuth = 0°

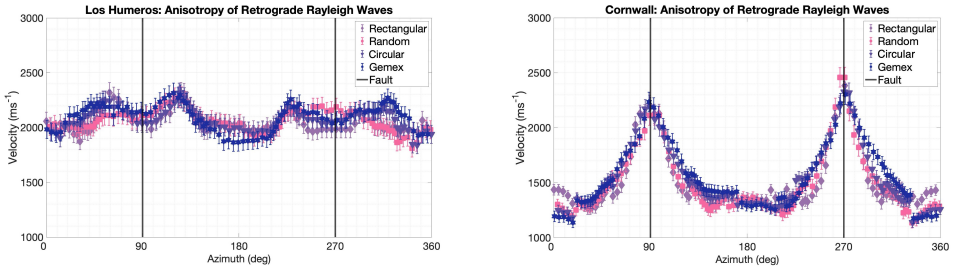

(a) Model of Los Humeros (b) Model of Cornwall

Figure A.18: Azimuth of source vs velocity plots for Retrograde Rayleigh waves for all array designs, for (a) conceptual model of Los Humeros and (b) conceptual model of Cornwall. Azimuth steps are 2.3°, 270° is parallel to faults, and 0° is perpendicular to faults. Black lines depict the fault strike.

The magnitude of anisotropy (a_{mag}) was calculated using half the difference between the fastest and the slowest velocities as a percentage of the sum of the percentage of the isotropic velocity [20].

Array	$a_{mag}(\%)$	a_0	a_1	a_2	a_3	a_4
Rectangular	2.473	2.034	-0.034	0.005	-0.021	-0.014
Random	4.668	2.063	-0.086	-0.004	0.011	-0.022
Circular	5.798	2.073	-0.063	0.012	-0.079	0.005
GEMex	7.386	2.087	-0.105	0.019	-0.082	0.003

Table A.2: Anisotropy parameters and magnitude of anisotropy (a_{mag}) for the different array designs for the model of Los Humeros, Fig.10(a).

Array	$a_{mag}(\%)$	a_0	a_1	a_2	a_3	a_4
Rectangular	23.004	1.544	-0.254	-0.042	0.222	0.060
Random	21.287	1.442	-0.216	-0.112	0.136	0.072
Circular	28.349	1.528	-0.344	0.056	0.199	0.059
GEMex	23.096	1.629	-0.1923	-0.086	0.241	0.0416

Table A.3: Anisotropy parameters and magnitude of anisotropy (a_{mag}) for the different array designs for the model of Cornwall, Fig.10(b).

Velocity Difference (ms^{-1})	$a_{mag}(\%)$	a_0	a_1	a_2	a_3	a_4
1400	4.622	2.464	0.022	0.017	-0.130	0.027
1500	4.566	2.457	0.014	0.023	-0.132	0.059
1600	5.612	2.090	-0.115	0.017	-0.030	0.079
1700	4.016	2.376	0.028	0.010	-0.035	0.016
2000	7.591	2.280	-0.059	0.006	0.060	-0.010

Table A.4: Anisotropy parameters and magnitude of anisotropy (a_{mag}) for the GEMex array for the different velocity variations.

References

[1] N. Riahi, G. Bokelmann, P. Sala, E. H. Saenger, Time-lapse analysis of ambient surface wave anisotropy: A three-component array study above an underground gas storage, Journal of Geophysical Research: Solid Earth 118 (10) (2013) 5339–5351.

[2] N. Bartels, G. Bussmann, R. Ignacy, Geothermal energy in the context of the energy transition process, in: 2018 International IEEE Conference and Workshop in Óbuda on Electrical and Power Engineering (CANDO-EPE), IEEE, 2018, pp. 000103–000108.

[3] G. Norini, G. Groppelli, R. Sulpizio, G. Carrasco-Núñez, P. Dávila-Harris, C. Pellicioli, F. Zucca, R. De Franco, Structural analysis and thermal remote sensing of the los humeros volcanic complex: Implications for volcano structure and geothermal exploration, Journal of Volcanology and Geothermal Research 301 (2015) 221–237.

[4] J. F. Bauer, M. Krumbholz, S. Meier, D. C. Tanner, Predictability of properties of a fractured geothermal reservoir: the opportunities and limitations of an outcrop analogue study, Geothermal Energy 5 (1) (2017) 1–27.

[5] N. Wang, J.-P. Montagner, G. Burgos, Y. Capdeville, D. Yu, Intrinsic versus extrinsic seismic anisotropy: Surface wave phase velocity inversion, Comptes Rendus. Géoscience 347 (2) (2015) 66–76.

[6] H. Kennedy, K. Löer, A. Gilligan, Constraints on fracture distribution in the los humeros geothermal field from beamforming of ambient seismic noise, Solid earth 13 (12) (2022) 1843–1858.

[7] S. Luo, H. Yao, Multistage tectonic evolution of the tanlu fault: Insights from upper crustal azimuthal anisotropy of the chao lake segment, Tectonophysics 806 (2021) 228795.

[8] Z. Li, Z. Peng, Stress-and structure-induced anisotropy in southern california from two decades of shear wave splitting measurements, Geophysical Research Letters 44 (19) (2017) 9607–9614.

[9] N. L. Boness, M. D. Zoback, Mapping stress and structurally controlled crustal shear velocity anisotropy in california, Geology 34 (10) (2006) 825–828.

[10] Z. Liu, J. Huang, H. Yao, Anisotropic rayleigh wave tomography of northeast china using ambient seismic noise, Physics of the Earth and Planetary Interiors 256 (2016) 37–48.

[11] A. Li, D. W. Forsyth, K. M. Fischer, Shear velocity structure and azimuthal anisotropy beneath eastern north america from rayleigh wave inversion, Journal of Geophysical Research: Solid Earth 108 (B8) (2003).

[12] C. P. Legendre, L. Zhao, W.-G. Huang, B.-S. Huang, Anisotropic rayleigh-wave phase velocities beneath northern vietnam, Earth, Planets and Space 67 (2015) 1–16.

[13] S. Crampin, Shear-wave splitting: new geophysics and earthquake stress-forecasting, Encyclopedia of Solid Earth Geophysics (2020) 1–11.

[14] R. T. Lacoss, E. J. Kelly, M. N. Toksöz, Estimation of seismic noise structure using arrays, Geophysics 34 (1) (1969) 21–38.

[15] J. Capon, High-resolution frequency-wavenumber spectrum analysis, Proceedings of the IEEE 57 (8) (1969) 1408–1418.

[16] C. Esmersoy, V. Cormier, M. Toksöz, Three-component array processing, the vela program: A twenty-five year review of basic research a, AV Kerr (1985) 565–578.

[17] R. Schmidt, Multiple emitter location and signal parameter estimation, IEEE transactions on antennas and propagation 34 (3) (1986) 276–280.

[18] K. Löer, B3AM: MATLAB toolbox for three-component beamforming (1.0), Zenodo. Available at `https://doi.org/10.5281/zenodo.10885984`, retrieved March 27, 2024. (2024).

[19] S. Rost, C. Thomas, Array seismology: Methods and applications, Reviews of geophysics 40 (3) (2002) 2–1.

[20] K. Löer, N. Riahi, E. H. Saenger, Three-component ambient noise beamforming in the parkfield area, Geophysical Journal International 213 (3) (2018) 1478–1491.

[21] E. H. Saenger, N. Gold, S. A. Shapiro, Modeling the propagation of elastic waves using a modified finite-difference grid, Wave motion 31 (1) (2000) 77–92.

[22] T. Bohlen, E. H. Saenger, Accuracy of heterogeneous staggered-grid finite-difference modeling of rayleigh waves, Geophysics 71 (4) (2006) T109–T115.

[23] L. M. Weydt, K. Bär, I. Sass, Petrophysical characterization of the los humeros geothermal field (mexico): from outcrop to parametrization of a 3d geological model, Geothermal Energy 10 (1) (2022) 5.

[24] K. E. Schulz, K. Bär, I. Sass, Lab-scale permeability enhancement by chemical treatment in fractured granite (cornubian batholith) for the united downs deep geothermal power project, cornwall (uk), Geosciences 12 (1) (2022) 35.

[25] M. Takarli, W. Prince, Permeability and p-wave velocity change in granitic rocks under freeze–thaw cycles, Geomechanics and Geoengineering: An International Journal 2 (3) (2007) 227–234.

[26] R. Scrivener, D. Highley, D. Cameron, K. Linley, R. White, Mineral resource information for development plans phase one cornwall: Resources and constraints (1997).

[27] M. A. Kassab, A. Weller, Study on p-wave and s-wave velocity in dry and wet sandstones of tushka region, egypt, Egyptian Journal of Petroleum 24 (1) (2015) 1–11.

[28] GPG, Seismic velocities of rocks and various materials, available at `https://gpg.geosci.xyz/content/physical_properties/tables/seismic_velocity.html` (2024).

[29] Eden Geothermal Limited, Eden geothermal – unlocking the energy from the rocks beneath our feet, available at `https://www.edengeothermal.com/` (Mar 2024).

[30] L. Ferrari, T. Orozco-Esquivel, V. Manea, M. Manea, The dynamic history of the trans-mexican volcanic belt and the mexico subduction zone, Tectonophysics 522 (2012) 122–149.

[31] E. Jolie, D. Bruhn, A. L. Hernández, D. Liotta, V. H. Garduño-Monroy, M. Lelli, G. P. Hersir, C. Arango-Galván, D. Bonté, P. Calcagno, P. Deb, C. Clauser, E. Peters, A. F. H. Ochoa, E. Huenges, Z. I. G. Acevedo, K. Kieling, E. Trumpy, J. Vargas, L. C. Gutiérrez-Negrín, A. Aragón-Aguilar, S. Halldórsdóttir, E. G. Partida, GEMex - A Mexican-European Research Cooperation on Development of Superhot and Engineered Geothermal Systems - Proceedings, Stanford, CA, USA, 2018.

[32] E. Fuentes-Guzmán, E. González-Partida, A. Camprubí, G. Hernández-Avilés, J. Gabites, A. Iriondo, G. Ruggieri, M. López-Martínez, The miocene tatatila-las minas iocg skarn deposits (veracruz) as a result of adakitic magmatism in the trans-mexican volcanic belt, Boletín de la Sociedad Geológica Mexicana 72 (3) (2020).

[33] M. H. P. Bott, A. Day, D. Masson-Smith, The geological interpretation of gravity and magnetic surveys in devon and cornwall, Philosophical Transactions of the Royal Society of London. Series A, Mathematical and Physical Sciences 251 (992) (1958) 161–191.

[34] D. Beamish, J. Busby, The cornubian geothermal province: heat production and flow in sw england: estimates from boreholes and airborne gamma-ray measurements, Geothermal Energy 4 (2016) 1–25.

[35] C. C. Hawley, Geology and Beryllium Deposits of the Lake George (or Badger Flats) Beryllium Area, Park and Jefferson Counties, Colorado, United States Department of the Interior. United States Government Publishing Office, A23, 1969.

[36] D. Manning, C. Exley, The origins of late-stage rocks in the st austell granite—a re-interpretation, Journal of the Geological Society 141 (3) (1984) 581–591.

[37] S. Camm, The Geology and Landscape of Cornwall and the Isles of Scilly, Alison Hodge Publishers, 2011.

[38] B. W. Chappell, R. Hine, The cornubian batholith: an example of magmatic fractionation on a crustal scale, Resource Geology 56 (3) (2006) 203–244.

[39] J. Capon, R. J. Greenfield, R. J. Kolker, Multidimensional maximum-likelihood processing of a large aperture seismic array, Proceedings of the IEEE 55 (2) (1967) 192–211.

[40] M. Gal, A. M. Reading, N. Nakata, L. Gualtieri, A. Fichtner, Beamforming and polarization analysis, Seismic ambient noise (2019) 32–72.

[41] K. Löer, T. Toledo, G. Norini, X. Zhang, A. Curtis, E. H. Saenger, Imaging the deep structures of los humeros geothermal field, mexico,

using three-component seismic noise beamforming, Seismological Society of America 91 (6) (2020) 3269–3277.

[42] P. Naghshin, H. Bahadori, Automatic extraction of retrograde and prograde rayleigh waves from three-component earthquake signals in different depths of earth, Soil Dynamics and Earthquake Engineering 147 (2021) 106800.

[43] S. Shaw, M. I. Othman, Characteristics of rayleigh wave propagation in orthotropic magneto-thermoelastic half-space: An eigen function expansion method, Applied Mathematical Modelling 67 (2019) 605–620.

[44] M. L. Smith, F. Dahlen, The azimuthal dependence of love and rayleigh wave propagation in a slightly anisotropic medium, Journal of Geophysical Research 78 (17) (1973) 3321–3333.

[45] J. Schweitzer, J. Fyen, S. Mykkeltveit, S. J. Gibbons, M. Pirli, D. Kühn, T. Kværna, Seismic arrays, in: New manual of seismological observatory practice 2 (NMSOP-2), Deutsches GeoForschungsZentrum GFZ, 2012, pp. 1–80.

[46] L. Lu, K. Wang, Z. Ding, The effect of uneven noise source and/or station distribution on the estimation of azimuth anisotropy of surface waves, Earthquake Science 31 (4) (2018) 175–186.

[47] S. Foti, F. Hollender, F. Garofalo, D. Albarello, M. Asten, P.-Y. Bard, C. Comina, C. Cornou, B. Cox, G. Di Giulio, et al., Guidelines for the good practice of surface wave analysis: a product of the interpacific project, Bulletin of Earthquake Engineering 16 (2018) 2367–2420.

[48] R. A. Haubrich, Array design, Bulletin of the Seismological Society of America 58 (3) (1968) 977–991.

[49] S. Mykkeltveit, K. Åstebøl, D. Doornbos, E. Husebye, Seismic array configuration optimization, Bulletin of the Seismological Society of America 73 (1) (1983) 173–186.

[50] A. K. Kerekes, Seismic array design by spatial convolution, Geophysics 66 (4) (2001) 1195–1207.

[51] K. Tokimatsu, J. Kōgakkai, I. S. of Soil Mechanics, E. G. E. Foundation Engineering. TC4, Geotechnical Site Characterization Using Surface Waves, 1995, available at https://books.google.co.uk/books?id=eobAGwAACAAJ.

[52] I. A. Beresnev, A. M. Nightengale, W. J. Silva, Properties of vertical ground motions, Bulletin of the Seismological Society of America 92 (8) (2002) 3152–3164.

[53] O. Nuttli, J. D. Whitmore, On the determination of the polarization angle of the s wave, Bulletin of the Seismological Society of America 52 (1) (1962) 95–107.

[54] T. Ikeda, T. Matsuoka, T. Tsuji, T. Nakayama, Characteristics of the horizontal component of rayleigh waves in multimode analysis of surface waves, Geophysics 80 (1) (2015) EN1–EN11.

[55] J. Xia, R. D. Miller, C. B. Park, Advantages of calculating shear-wave velocity from surface waves with higher modes, in: SEG technical program expanded abstracts 2000, Society of Exploration Geophysicists, 2000, pp. 1295–1298.

[56] J. Achenbach, Wave propagation in elastic solids, Elsevier, 1973.

[57] J. J. Zhang, L. R. Bentley, Factors determining poisson's ratio, CREWES Res Rep 17 (2005) 1–15.

[58] L. L. Lacy, Dynamic rock mechanics testing for optimized fracture designs, in: SPE Annual Technical Conference and Exhibition?, SPE, 1997, pp. SPE–38716.

[59] A. F. Siggins, Dynamic elastic tests for rock engineering, in: Rock Testing and Site Characterization, Elsevier, 1993, pp. 601–618.

[60] G. Hamada, Reservoir fluids identification using vp/vs ratio?, Oil & Gas Science and Technology 59 (6) (2004) 649–654.

[61] X.-Q. Wang, A. Schubnel, J. Fortin, E. David, Y. Guéguen, H.-K. Ge, High vp/vs ratio: Saturated cracks or anisotropy effects?, Geophysical Research Letters 39 (11) (2012).

[62] G. E. Backus, Possible forms of seismic anisotropy of the uppermost mantle under oceans, Journal of Geophysical Research 70 (14) (1965) 3429–3439.

[63] T. Ikeda, T. Tsuji, Azimuthal anisotropy of rayleigh waves in the crust in southern tohoku area, japan, Journal of Geophysical Research: Solid Earth 119 (12) (2014) 8964–8975.

[64] S. Schippkus, C. Hadziioannou, Matched field processing accounting for complex earth structure: method and review, Geophysical Journal International 231 (2) (2022) 1268–1282.

[65] K. Sager, L. Ermert, C. Boehm, A. Fichtner, Towards full waveform ambient noise inversion, Geophysical Journal International 212 (1) (2018) 566–590.

[66] J. Chaput, R. Aster, M. Karplus, N. Nakata, P. Gerstoft, P. Bromirski, A. Nyblade, R. Stephen, D. Wiens, Near-surface seismic anisotropy in antarctic glacial snow and ice revealed by high-frequency ambient noise, Journal of Glaciology 69 (276) (2023) 773–789.

[67] G. Norini, G. Carrasco-Núñez, F. Corbo-Camargo, J. Lermo, J. H. Rojas, C. Castro, M. Bonini, D. Montanari, G. Corti, G. Moratti, et al., The structural architecture of the los humeros volcanic complex and geothermal field, Journal of Volcanology and Geothermal Research 381 (2019) 312–329.